Supplementary Information

Empowering Soft Conductive Elastomers with Self-Reinforcement and Remarkable Resilience via Phase-Locking Ions

Kai Lu[1], Zaizheng Sun[1], Jinming Liu[1], Chengyi Huang[1,2], Dongsheng Mao[1], Haiming Chen[1,2,]*

1. Key Laboratory of Advanced Marine Materials, Ningbo Institute of Materials Technology and Engineering, Chinese Academy of Sciences, Ningbo, 315201, China
2. Laboratory of Polymers and Composites, Ningbo Institute of Materials Technology and Engineering, Chinese Academy of Sciences, Ningbo, 315201, China

Corresponding author (*):

Haiming Chen: chenhaiming@nimte.ac.cn

Supplementary Videos

Video S1. Powering bulbs at elevated temperatures and extinguishing them at lower temperatures.

Video S2. SRICE-10 is subjected to loads from several dumbbells of varying weights (5 kg to 20 kg), generating corresponding $\Delta R/R_0$ values for recording.

Video S3. Illuminating 100 bulbs when SRICE-10 is contact-separating with PTFE, the contact area is 20 mm × 20mm.

Video S4. Display of touching $1^{\#}$, $2^{\#}$, $3^{\#}$, $4^{\#}$ and $5^{\#}$ position, respectively.

Video S5. Display of sliding motion on the SRICE-10 strip.

Video S6. Display of playing "Go game" when SRICE-10 is used as a human-machine interaction node.

Supplementary Experimental

1. Materials

1-Ethyl-3-methylimidazolium bis(trifluoromethylsulfonyl)imide ($[EMIM]^+[TFSI]^-$), dibutyltin dilaurate (DBTDL), polytetramethylene ether glycol (PTMEG, Mn=2000 g/mol), adipic dihydrazide (AD) and 4,4'-methylenebis(cyclohexyl isocyanate) (HMDI) were purchased from Aladdin (Shanghai, China). Methanol (MeOH) and anhydrous dimethylformamide (DMF) were purchased from J&K scientific. All reagents were commercially available and used as supplied without further purification.

2. Elastomers preparation

First, PTMEG with preset content were filled into a three-necked flask and degassed a nitrogen atmosphere at for 1 hours (80 ºC). Next, anhydrous DMF (30 mL) and HMDI with preset content were added dropwise to trigger the reaction for 2 hours. Subsequently, the AD/DMF solution with corresponding content were added dropwise to the reaction flask. After the reaction, the solution was cooled down to 25 ºC while keeping stirring, and the $[EMIM]^+[TFSI]^-$ with preset content was added at 25 ºC. Finally, the obtained solution was poured into a Teflon dish and was de-bubbed before drying at 40 ºC in oven. The prepared solid specimens were cut into dumbbell shaped specimens with the size of 50 mm × 2 mm × 0.5 mm (length × width × thickness) for mechanical testing.

3. Characterization

Thermogravimetric Analyzer (TGA) experiments were carried out using a TA instruments' TGA Q500 with a heating rate of 20 °C/min at the range of 50 ~ 700 °C. Gel permeation chromatography (GPC) were performed on a HLC8320 GPC solvent/sample Module. HPLC grade DMF was used as eluent with a flow rate of 1.0 mL/min. Monodispersed poly(methyl methacrylate) standards were used to obtain a calibration curve. Differential scanning calorimetry (DSC) (DSC 214, NETZSCH, Germany) was carried out to investigate the thermal behavior with a heating/cooling rate of 10 °C/min in the range of -100~100 °C.

Rheological properties were performed on an oscillatory rheometer (Discovery HR 30, TA) using a 25 mm parallel plate-plate geometry. Prior to each experiment, approximately 1.2 mm thick film samples were prepared, and each film sample was placed between the parallel plates. A temperature-sweep

experiment was carried out between 80 and 220 °C at an ω and shear strain of 1 rad/s and 1%, respectively. In addition, frequency sweeping was carried out in the 0.1−100 rad/s ω range at a constant shear strain of 1%. The segmental relaxation behavior of each SRICE was examined on the basis of the relaxation time obtained from the frequency-sweep data:

$$\frac{G'}{(|\eta^*|\omega)^2} = \frac{\tau}{|\eta^*|} \qquad (1)$$

where G', η^*, and τ are the storage modulus, complex viscosity, and relaxation time, respectively. The τ_s was obtained from the τ value at 0.1 rad/s. Mechanical properties were tested at room temperature using a Zwick/Roell Z1.0 tensile machine at a specific crosshead speed illustrated in paper. Five specimens of each composition were tested, and the reported data was the average value.

In-situ wide angle X-ray scattering (WAXS) and small angle X-ray scattering (SAXS) were measured using the Xeuss 3.0 SAXS/WAXS system (Xenocs SA, France). Cu Kα X-ray source (GeniX3D Cu ULD), generated at 50 kV and 0.6 mA, was utilized to generate X-ray radiation with a wavelength of 1.5418 Å. Eiger 2R Hybrid pixel photon counting detector (500K model, vacuum compatible, windowless) with a silicon sensor at a thickness of 450 μm and a resolution of 512 × 1028 pixels (pixel size = 75 × 75 μm^2) was used to collect the scattered signals. Each SAXS pattern was collected with a 5-minute exposure. The one-dimensional intensity profiles were integrated from background corrected 2D SAXS patterns. The crystal size is calculated by the Scherrer equation: $D=\frac{K\lambda}{\beta\cos\theta}$, where D is the average size of the crystal domains and K is a dimensionless shape factor of approximately 0.89, β is the line broadening at half the maximum intensity (FWHM) after subtracting the instrumental line broadening, θ is the Bragg angle.

4. Electrical Measurement

Electrochemical impedance spectroscopy tests were performed using an electrochemical workstation (Zahner Zennium XC) over a frequency range of 1 MHz to 100 mHz with a perturbation voltage of 10 mV. The SRICE discs were assembled into CR2032 button cells in a standard stainless steel spacer/electrolyte/standard stainless steel spacer configuration inside a glove box filled with inert gas at an encapsulation pressure of 5 MPa. The assembled cells were then stored for 1 hour at 25°C.

The open circuit voltage (V_{oc}) and short-circuit current (I_{sc}) of TENG were measured by electrometer (Keithley 6514). The cyclic contact-separation action was conducted by a linear motor (LinMot B01-37x166/260) with a acceleration of 0.5 m s^{-2}. Teflon film attached to copper film was selected as the counterpart for cyclic contact-separating. Unless otherwise indicated, measurements were performed at room temperature under a gap distance of 4 cm and a frequency of 1 Hz. The conductivity was measured by Hall effect measurement system with a temperature controller (8404-CRX-6.5K, USA). The grid-free 2D position recognition sensor was fabricated just by connecting the sides (2 nodes) or the corners (4 nodes) of target films. The electric signal was recorded by data acquisition card (DAM-3059-V) and imaged via running a homemade software.

5. Molecular dynamics simulation

The binding energy of the corresponding chemical couples are calculated by the Materials Studio 8.0 software with the built-in Forcite module. Detailly, the chemical couples were constructed first and undergone the geometry optimization with the quality of fine in the forcefield of compass II, then the energy of the chemical couples (E_{total}) and each geometry optimized chemical (E_i) were calculated with the same quality and forcefield. As a consequently, the binding energy is:[1] $E_{couples} = \sum_{1}^{i} E_i - E_{total}$. The diffusion coefficient of ions is also simulated by the Forcite module in the forcefield of compass II. The constructed PU chain contains 6 HDMI units, 2 ADH units, and 4 PTMEG (in which contains 27 repeat units). The constructed amorphous cell contains 4 PU chains and the corresponding mass concentration of [EMIM][TFSI]. Then the constructed amorphous cell undergoes the geometry optimization and annealing. Finally, the mean square dispalcement is analyzed to calculate the diffusion coefficient of ions by[2]:

$D = \frac{1}{6N_\alpha} \lim_{t\to\infty} \frac{d}{dt} \sum_{i=1}^{N_\alpha} \left\langle [r_i(t) - r_i(0)]^2 \right\rangle$, where N_α is the number of ions.

Supplementary Figures

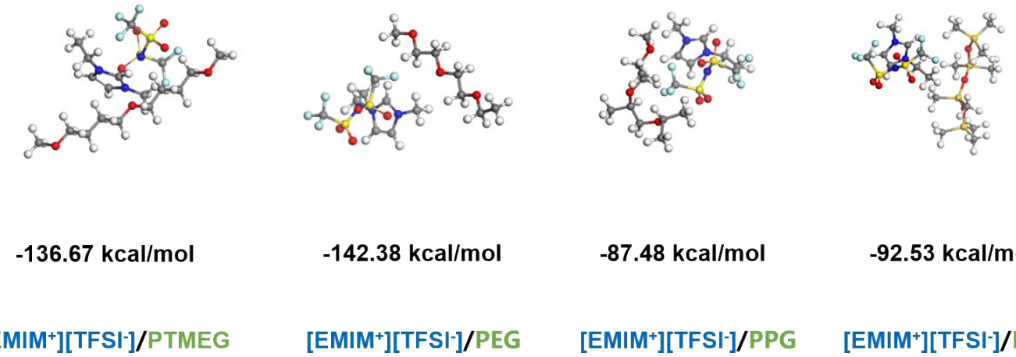

Figure S1. The binding energy of PCL/[EMIM][TFSI], PEG/[EMIM][TFSI], PPG/[EMIM][TFSI] and PDMS/[EMIM][TFSI] respectively.

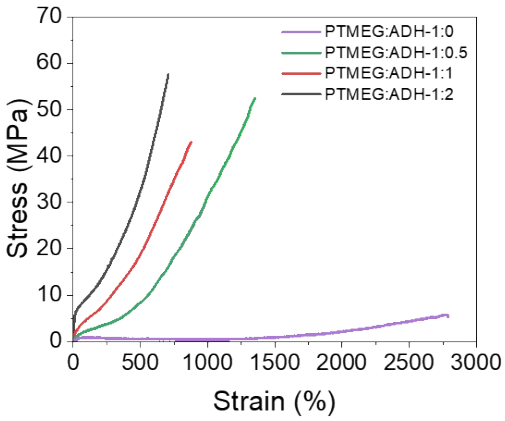

Figure S2. The typical engineering stress-strain curves of synthesized polyurethane elastomers with various ADH content.

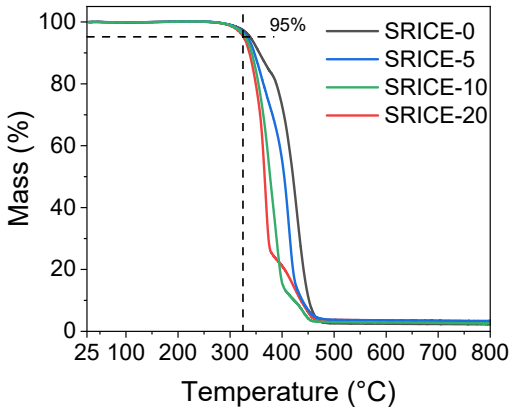

Figure S3. TGA curves show the mass evolution of SRICEs with temperature.

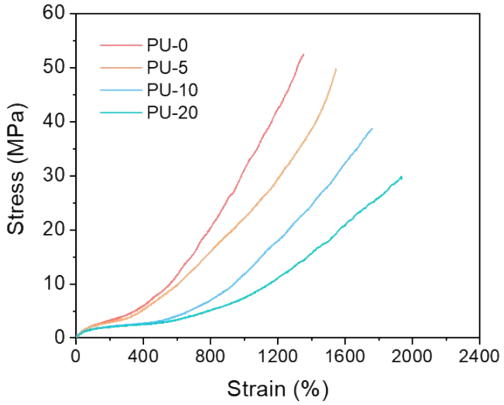

Figure S4. The typical engineering stress-strain curves of polyurethance elastomers coupled with $[EMIM]^{+}[TFSI]^{-}$ at 80°C.

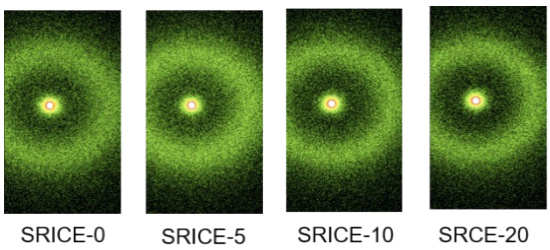

Figure S6. 2D SAXS patterns of SRICEs.

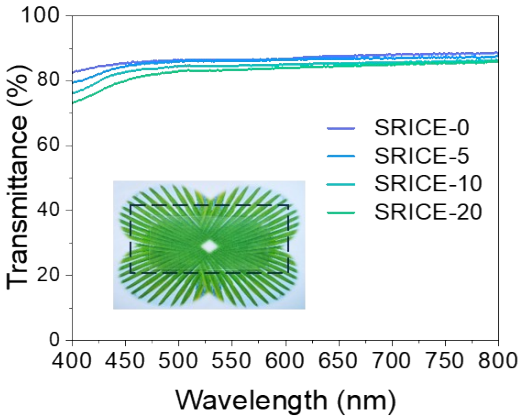

Figure S5. The transmittance of SRICEs in the whole visible range. The inset shows the image of SRICE-10 covered on colorful paper.

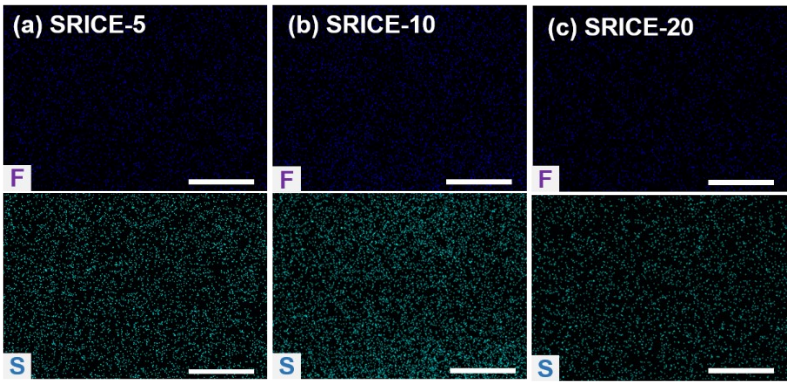

Figure S7. The energy dispersive X-ray spectroscopy (EDS) of SRICE-5 (a), SRICE-10 (b) and SRICE-20 (c) respectively, shows the F and S elements are well distributed in the whole view. Scale bar is 3 μm.

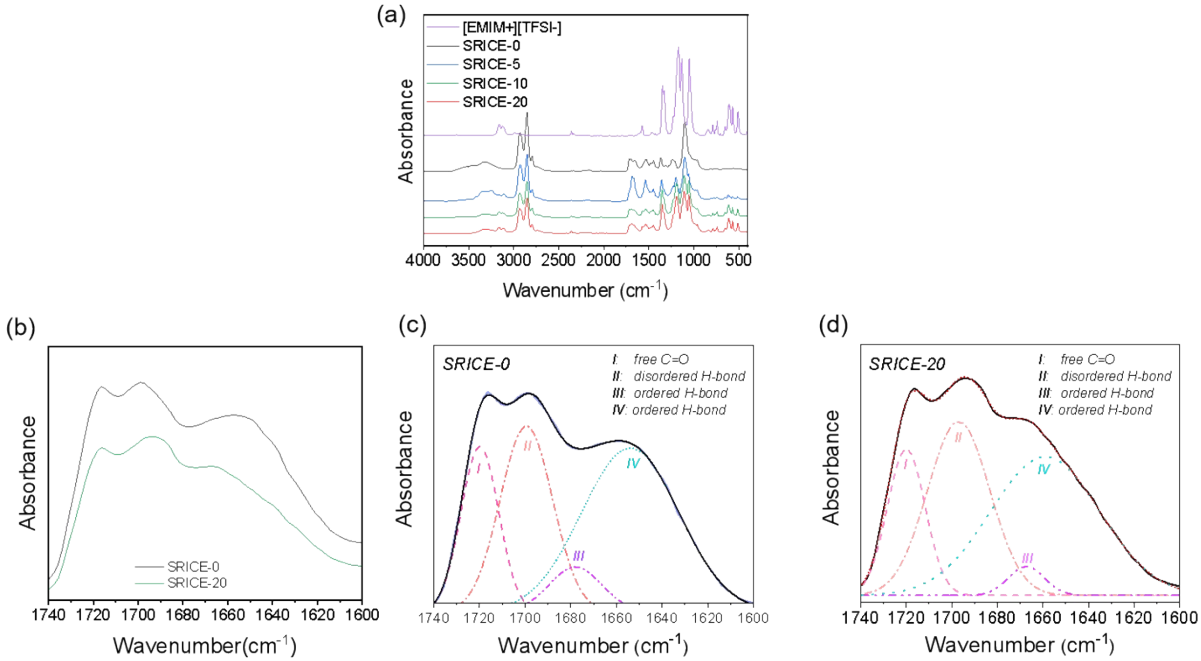

Figure S8. (a) FTIR spectra of SRICE. (b-d) show the C=O stretching vibration. (b) Comparison of SRICE-0 and SRICE-20. (c-d) The deconvoluted fittings of the C=O stretching vibration bands: (c) SRICE-0 and (d) SRICE-20. The fraction of hydrogen bonds is calculated by $f_{H-Bond} = (1 - \frac{A_I}{A_I + A_{II} + A_{III} + A_{IV}}) \times 100\%$, they are 81.87% and 83.00% for SRICE-0 and SRICE-20, respectively.

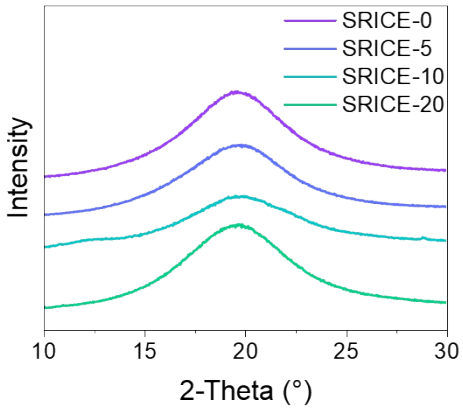

Figure S9. 1D WAXS profiles of SRICEs.

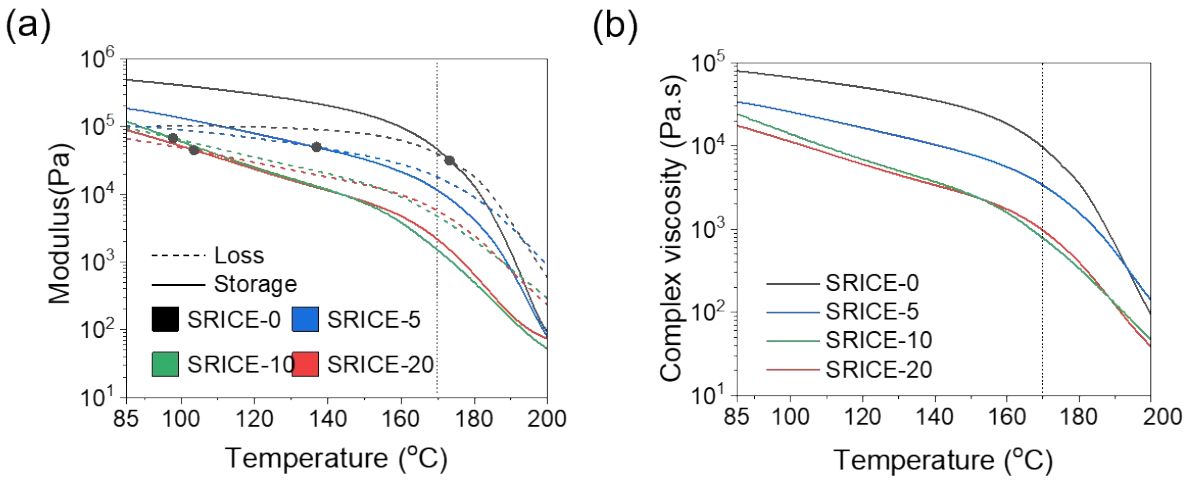

Figure S10. Rheological properties of **SRICEs.** (a) The modulus as a function of temperature of **SRICEs**. (b) The complex viscosity evolution with temperature.

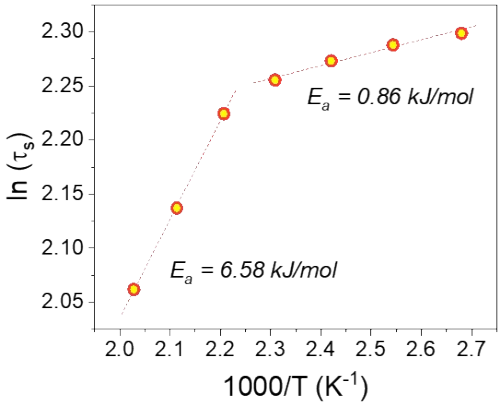

Figure S11. The relationship between characteristic relaxation time (ln (τ*)) and temperature of SRICE-0.

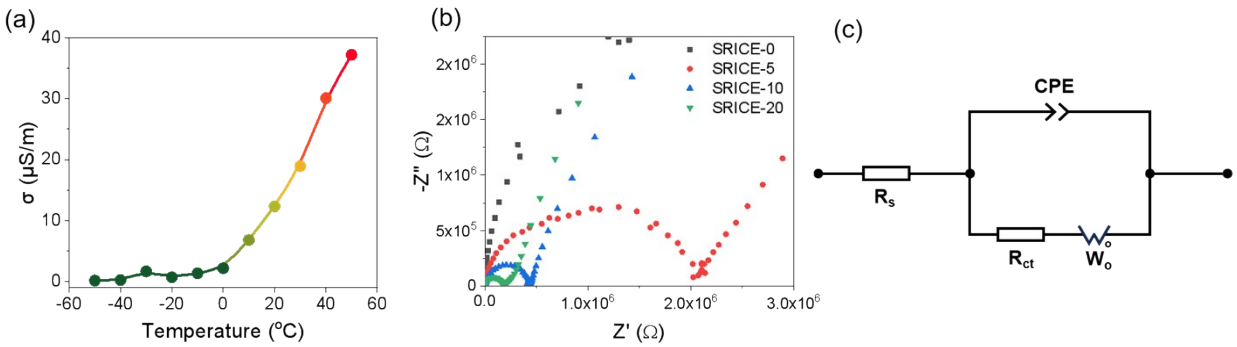

Figure S12. (a) The conductivity of SRICE-10 as a functional of temperature. (b) Electrochemical impedance spectroscopy of SRICE and (c) their equivalent circuit.

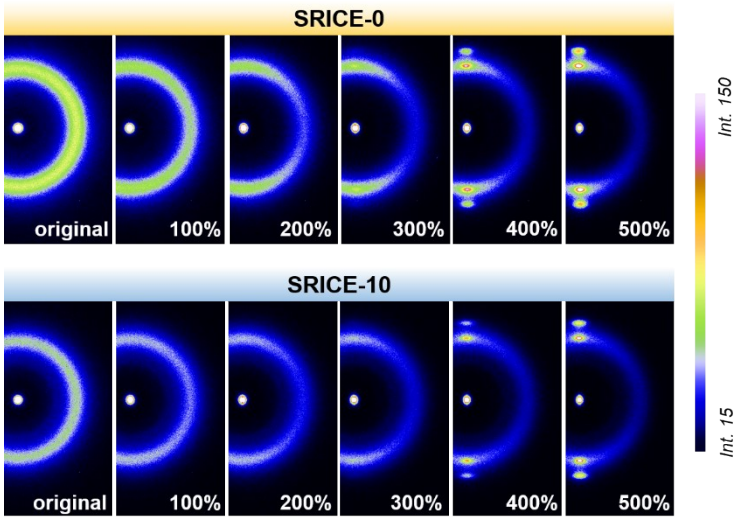

Figure S13. 2D WAXS patterns of SRICE-0 and SRICE-10 captured at different strains as indicated in picture. The stretching direction is vertical.

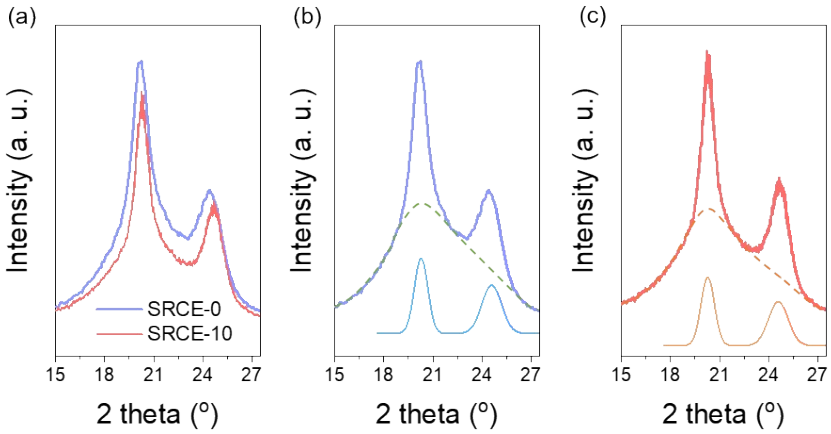

Figure S14. (a) Comparison of the experimental diffraction profiles of SRICE-0 and SRICE-10. (b-c) The experimental profile, fitted amorphous halo (dash line) and fitted crystalline peak (solid line) of (b) SRICE-0 and (c) SRICE-10, respectively.

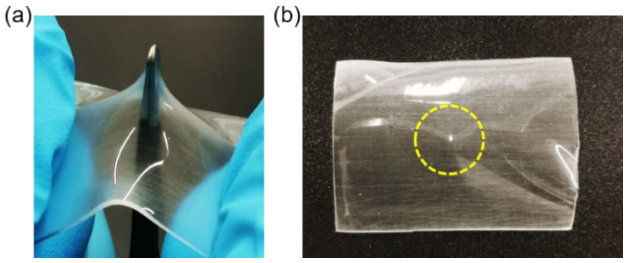

Figure S15. Digital images of (a) poking SRICE-10 with a tweezer and (b) it recovers instantly once releasing the stress.

Supplementary Note

Power generation mechanism of SRICE-10:

Figure S16 shows the power generation mechanism of SRICE-10. The stable addition of $[EMIM]^+[TFSI]^-$ allowed the PU matrix not only acts as a dielectric layer for contact electrification when contacted with external matters but also an ion conducting layer for electrostatic induction. Initially, the SRICE-10 and polytetrafluoroethylene (PTFE, a typical polymer with triboelectric negativity) film are spaced apart from each other, so they exhibit electrical neutralization (i). When they approach and are contacted, electrons are transferred from the surface of PU matrix to that of PTFE due to the difference in their electron affinities, namely contact electrification (ii). After then detaching, the positive charges that have accumulated on the surface of PU matrix create an electric field that draws anions to such surface. At this point, an electrical double layer (EDL) is created between the accumulated positive charges and the drawn anions. Meanwhile, cations are repelled and another EDL is created at the interface between the SRICE-10 and the inserted metal wire, where the cations accumulated in the EDL attract electrons from the ground through the inserted metal wire, namely electrostatic induction (iii). When the electrically charged PTFE approaches the SRICE-10 again, the electric field in the SRICE-10 diminishes and the ions in the SRICE-10 are rearranged. As a result, the induced electrons flow back to the opposite direction (iv). Therefore, there is a significant relationship between the frequency of contact-separation and the output performance. The output voltage is frequency-independent at lower frequencies of <1 Hz because there is enough time for the ions to rearrange and the integrated electric field to vanish. But the complete rearrangement of oriented ions is challenging when the contact-separation frequency >1 Hz, which raises the output voltage. Additionally, the accumulated charges and the output voltage are strongly dependent on the content of PU matrix, which are slightly decreases with $[EMIM]^+[TFSI]^-$. Similarly, thinning SRICE-10 would conducive to the generation of EDL, thereby producing a larger output voltage.

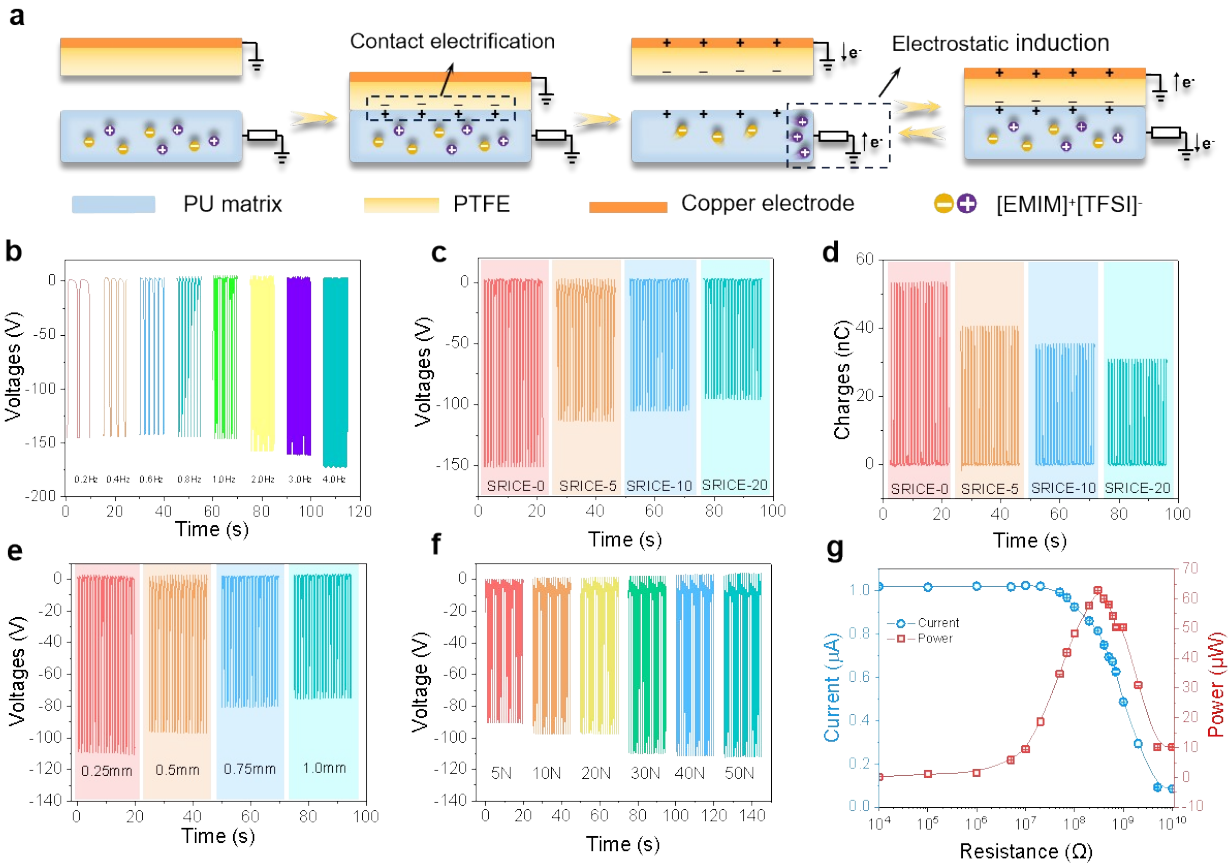

Figure S16. Triboresistance performance of SRICEs. (a) Power generation mechanism of SRICE-10. (b) The relationship of contact-separation frequency and output voltages. (c) Generated voltages and (d) accumulated charges of SRICEs, respectively. (e) Output voltages of SRICE-10 with different thickness. (f) Relationship between contact pressure and output voltage. (g) Current and power when loading resistors from 10 kΩ to 10 GΩ in series. The contact area is 20 mm × 20mm unless otherwise specified.

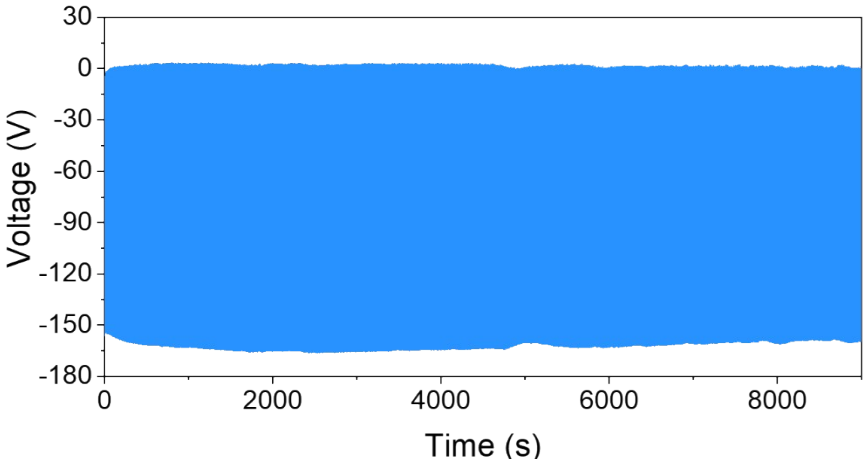

Figure S17. The output voltages of SRICE-10 performed during consecutive cycling of contact-separating with PTFE at a contact area of 2.5 cm × 2.5 cm and a frequency of 2 Hz.

Supplementary Tables

Table S1. Mechanical properties comparison of SRICEx and literature-reported ion-conductive elastomers.

Samples	Crosslinkers	Strength (MPa)	Modulus (MPa)	Toughness (MJ/m^3)	References
SRICE-5	H-bonds	53.3	5.23	198.6	This work
SRICE-10	H-bonds	51.0	5.00	202.4	This work
SRICE-20	H-bonds	49.3	4.98	195.3	This work
M-gel (cellulose)	H-bonds	6.52	31.5	1.54	[3]
hydrogels (cellulose)	H-bonds	47	140	20	[4]
ionic conductive elastomers (ICE)	H-bonds	11.9	0.87	162	[5]
DSICE	H-bonds	27.83		164.36	[6]
supramolecular ionic networks	H-bonds, ionic coordination and crystals	53.5	60.3		[7]
ionic conductive elastomers (ICE)	H-bonds and Electrostatic force	0.9	7.12	35	[8]
ionic conductive elastomers (ICE)	H-bonds and Electrostatic force	0.75	0.1	4.65	[9]
PTFEA	H-bonds and Electrostatic force	0.72		3.66	[10]
ion-conducting fluorinated elastomer (ICFE)	Electrostatic force	0.77		17.1	[11]
SOTG	Electrostatic force	5.19		50	[12]
IG	Electrostatic force	11	337		[13]
IG	Electrostatic force	10.1	82.8		[14]
cellulose hydrogels	ionic coordination	8.7		1.6	[15]
OG-[M]	Metal coordination bond	14.3	55	78	[16]
MOF-ionogels	MOF metal sites	7.6	58	21	[17]
PS-NCC (cellulose)	nanocrystalline	5.92	44	34	[18]
PU	Chemistry crosslinker,	2.52	1.43		[19]

F/PAA DN gel	Chemistry crosslinker,	1.04	2.32	1.07	[20]
hydrogels	Chemistry crosslinker	1.3		7.34	[21]
hydrogels	Chemistry crosslinker	0.26		0.154	[22]
hydrogels	Chemistry crosslinker	0.4		1.5	[23]
Polymerizable deep eutectic solvent	Chemistry crosslinker	0.33	0.17	3.4	[24]

Table S2. Resilient efficiency comparison of SRICEx and literature-reported ion-conductive elastomers.

Samples	Crosslinkers	ε_{max}（%）	Resilient efficiency (%)	References
SRICE-10	H-bonds	600	92.5	This work
IPB-3-30IL	H-bonds	100	85	[25]
PVA-PAA	H-bonds	200	42.5	[26]
I40-SS-CPU	H-bonds	200	65	[27]
WE-30	H-bonds	100	90	[28]
ntf2	H-bonds and Electrostatic force	100	87	[29]
IG10255	H-bonds and Electrostatic force	100	50	[30]
IG70%-10%	Electrostatic force	600	91.7	[31]
1% HPC ionogel	Electrostatic force	300	86.7	[32]
PU-IL_2	H-bonds	200	87.5	[33]
EA-PR-IL-100%	slidable cross-linkers	100	82	[34]
SIG	Electrostatic force	100	78	[35]
IG2560	Chemistry crosslinker	100	88	[36]
I-2%	H-bonds and Electrostatic force	400	70	[37]
ionogel-2	H-bonds and Electrostatic force	500	78	[38]
ICE-0.5 m	H-bonds and Electrostatic force	500	85	[39]
PU-$DES_{40\%}$	Electrostatic force	200	72.5	[40]
ND-1-1	H-bonds	300	68.3	[41]

Supplementary References

(1) Wang, L.; Guo, L.; Zhang, K.; Xia, Y.; Hao, J.; Wang, X. Development of Tough Thermoplastic Elastomers by Leveraging Rigid–Flexible Supramolecular Segment Interplays. *Angew. Chem. Int. Ed.* **2023**, *62* (29), e202301762.

(2) Meunier, M. Diffusion coefficients of small gas molecules in amorphous cis-1,4-polybutadiene estimated by molecular dynamics simulations. *J. Chem. Phys.* **2005**, *123*. 134906.

(3) Cao, K.; Zhu, Y.; Zheng, Z.; Cheng, W.; Zi, Y.; Zeng, S.; Zhao, D.; Yu, H. Bio-Inspired Multiscale Design for Strong and Tough Biological Ionogels. *Adv. Sci.* **2023**, *10*, 2207233.

(4) Mredha, M. T. I.; Le, H. H.; Tran, V. T.; Trtik, P.; Cui, J.; Jeon, I. Anisotropic tough multilayer hydrogels with programmable orientation. *Mater. Horiz.* **2019**, *6*, 1504-1511.

(5) Mackanic, D. G.; Yan, X.; Zhang, Q.; Matsuhisa, N.; Yu, Z.; Jiang, Y.; Manika, T.; Lopez, J.; Yan, H.; Liu, K.; et al. Decoupling of mechanical properties and ionic conductivity in supramolecular lithium ion conductors. *Nat. Commun.* **2019**, *10*, 5384.

(6) Chen, J.; Gao, Y.; Shi, L.; Yu, W.; Sun, Z.; Zhou, Y.; Liu, S.; Mao, H.; Zhang, D.; Lu, T.; et al. Phase-locked constructing dynamic supramolecular ionic conductive elastomers with superior toughness, autonomous self-healing and recyclability. *Nat. Commun.* **2022**, *13*, 4868.

(7) Li, W.; Li, L.; Liu, Z.; Zheng, S.; Li, Q.; Yan, F. Supramolecular Ionogels Tougher than Metals. *Adv. Mater.* **2023**, *35*, 2301383.

(8) Yiming, B.; Han, Y.; Han, Z.; Zhang, X.; Li, Y.; Lian, W.; Zhang, M.; Yin, J.; Sun, T.; Wu, Z.; et al. A Mechanically Robust and Versatile Liquid-Free Ionic Conductive Elastomer. *Adv. Mater.* **2021**, *33* (11), 2006111.

(9) Yiming, B.; Guo, X.; Ali, N.; Zhang, N.; Zhang, X.; Han, Z.; Lu, Y.; Wu, Z.; Fan, X.; Jia, Z.; et al. Ambiently and Mechanically Stable Ionogels for Soft Ionotronics. *Adv. Funct. Mater.* **2021**, *31* (33), 2102773

(10) Xu, L.; Huang, Z.; Deng, Z.; Du, Z.; Sun, T. L.; Guo, Z.-H.; Yue, K. A Transparent, Highly Stretchable, Solvent-Resistant, Recyclable Multifunctional Ionogel with Underwater Self-Healing and Adhesion for Reliable Strain Sensors. *Adv. Mater.* **2021**, *33* (51), 2105306.

(11) Shi, P.; Wang, Y.; Wan, K.; Zhang, C.; Liu, T. A Waterproof Ion-Conducting Fluorinated Elastomer with 6000% Stretchability, Superior Ionic Conductivity, and Harsh Environment Tolerance. *Adv. Funct. Mater.* **2022**, *32* (22), 2112293.

(12) Gong, Y.; Li, Z.; Li, H.; Wu, W.; Zhou, W.; Zhao, J.; He, C.; Jiang, M. Ultra-Tough Room-Temperature Dielectric Switching Ionic Gels with Long-Cycle Stability. *Adv. Funct. Mater.* **2022**, *32* (45), 2207452.

(13) Yu, Z.; Wu, P. Water-Resistant Ionogel Electrode with Tailorable Mechanical Properties for Aquatic Ambulatory Physiological Signal Monitoring. *Adv. Funct. Mater.* **2021**, *31* (51), 2107226

(14) Yu, Z.; Wu, P. Underwater Communication and Optical Camouflage Ionogels. *Adv. Mater.* **2021**, *33* (24), 2008479.

(15) Zhou, S.; Guo, K.; Bukhvalov, D.; Zhu, W.; Wang, J.; Sun, W.; He, M. H-bond/ionic coordination switching for fabrication of highly oriented cellulose hydrogels. *J. Mater. Chem. A* **2021**, *9* (9), 5533-5541.

(16) Li, L.; Li, W.; Wang, X.; Zou, X.; Zheng, S.; Liu, Z.; Li, Q.; Xia, Q.; Yan, F. Ultra-Tough and Recyclable Ionogels Constructed by Coordinated Supramolecular Solvents. *Angew. Chem. Int. Ed.* **2022**, *61* (50), e202212512.

(17) Xia, Q.; Li, W.; Zou, X.; Zheng, S.; Liu, Z.; Li, L.; Yan, F. Metal–organic framework (MOF) facilitated highly stretchable and fatigue-resistant ionogels for recyclable sensors. *Mater. Horiz.* **2022**, *9* (11), 2881-2892.

(18) Shan, C.; Che, M.; Cholewinski, A.; Su, R.; Zhao, B. Multifunctional nanocrystalline cellulose ionogels toward tough and sustainable materials. *Cell Reports Phys. Sci.* **2023**, *4* (8).

(19) Li, T.; Wang, Y.; Li, S.; Liu, X.; Sun, J. Mechanically Robust, Elastic, and Healable Ionogels for Highly Sensitive

Ultra-Durable Ionic Skins. *Adv. Mater.* **2020**, *32* (32), 2002706.
(20) Quan, Q.; Fan, C.; Pan, N.; Zhu, M.; Zhang, T.; Wang, Z.; Dong, Y.; Wu, Y.; Tang, M.; Zhou, X.; et al. Tough and Stretchable Phenolic-Reinforced Double Network Deep Eutectic Solvent gels for Multifunctional Sensors with Environmental Adaptability. *Adv. Funct. Mater.* **2023**, *33* (36), 2303381.
(21) Fu, M.; Sun, Z.; Liu, X.; Huang, Z.; Luan, G.; Chen, Y.; Peng, J.; Yue, K. Highly Stretchable, Resilient, Adhesive, and Self-Healing Ionic Hydrogels for Thermoelectric Application. *Adv. Funct. Mater.* **2023**, *33* (43), 2306086.
(22) Xiang, C.; Wang, Z.; Yang, C.; Yao, X.; Wang, Y.; Suo, Z. Stretchable and fatigue-resistant materials. *Mater. Today* **2020**, *34*, 7-16.
(23) Morelle, X. P.; Illeperuma, W. R.; Tian, K.; Bai, R.; Suo, Z.; Vlassak, J. J. Highly Stretchable and Tough Hydrogels below Water Freezing Temperature. *Adv. Mater.* **2018**, *30* (35), 1801541.
(24) Zhang, X.; Fu, Q.; Wang, Y.; Zhao, H.; Hao, S.; Ma, C.; Xu, F.; Yang, J. Tough Liquid-Free Ionic Conductive Elastomers with Robust Adhesion and Self-Healing Properties for Ionotronic Devices. *Adv. Funct. Mater.* **2024**, *34* (4), 2307400.
(25) Zhang, Z.; Qian, L.; Cheng, J.; Ma, C.; Zhang, G. Neural Network-Inspired Polyurea Ionogel with Mechanical Robustness, Low Hysteresis, and High Transparency for Soft Iontronics. *Adv. Funct. Mater.* **2024**, *34(4),* 2402115.
(26) Wang, Y.; Wei, Z.; Ji, T.; Bai, R.; Zhu, H. Highly Ionic Conductive, Stretchable, and Tough Ionogel for Flexible Solid-State Supercapacitor. *Small* **2023**, 2307019.
(27) Yang, L.; Sun, L.; Huang, H.; Zhu, W.; Wang, Y.; Wu, Z.; Neisiany, R. E.; Gu, S.; You, Z. Mechanically Robust and Room Temperature Self-Healing Ionogel Based on Ionic Liquid Inhibited Reversible Reaction of Disulfide Bonds. *Adv. Sci.* **2023**, *10* (20), 2207527.
(28) Wen, X.; Xu, J.; Wang, H.; Du, Z.; Wang, S.; Cheng, X. High strength, self-healing, and anti-freezing polyurethane ionogel based on multiple hydrogen bonding for wearable strain sensor. *Polym. Eng. Sci.* **2022**, *62* (10), 3132-3143.
(29) Zhao, Y.; Gan, D.; Wang, L.; Wang, S.; Wang, W.; Wang, Q.; Shao, J.; Dong, X. Ultra-Stretchable, Adhesive, and Anti-Swelling Ionogel Based on Fluorine-Rich Ionic Liquid for Underwater Reliable Sensor. *Adv. Mater. Tech.* **2023**, *8* (7), 2201566.
(30) Jin, Z.; Liu, H.; Zhang, H. Environment Endurable, Self-Healing, Super-Adhesive, and Mechanically Strong Ionogels for Reliable Sensing. *Macromol. Rapid Commun.* **2024**, *45* (2), 2300457.
(31) Zhang, M.; Yu, R.; Tao, X.; He, Y.; Li, X.; Tian, F.; Chen, X.; Huang, W. Mechanically Robust and Highly Conductive Ionogels for Soft Ionotronics. *Adv. Funct. Mater.* **2023**, *33* (10), 2208083.
(32) Wang, Y.; Sun, S.; Wu, P. Adaptive Ionogel Paint from Room-Temperature Autonomous Polymerization of α-Thioctic Acid for Stretchable and Healable Electronics. *Adv. Funct. Mater.* **2021**, *31* (24), 2101494.
(33) Li, T.; Wang, Y.; Li, S.; Liu, X.; Sun, J. Mechanically Robust, Elastic, and Healable Ionogels for Highly Sensitive Ultra-Durable Ionic Skins. *Adv. Mater.* **2020**, *32* (32), 2002706.
(34) Du, R.; Bao, T.; Zhu, T.; Zhang, J.; Huang, X.; Jin, Q.; Xin, M.; Pan, L.; Zhang, Q.; Jia, X. A Low-Hysteresis and Highly Stretchable Ionogel Enabled by Well Dispersed Slidable Cross-Linker for Rapid Human-Machine Interaction. *Adv. Funct. Mater.* **2023**, *33* (30), 2212888.
(35) Jia, L.; Xiao, J.; Tan, Y.; Zhang, K.; Liu, Y.; Wang, X. Supramolecular Ionogels for Use in Locating Damage to Underwater Infrastructure. *Small* **2023**, 2309231.
(36) Sun, Y.; Huang, J.; Cheng, Y.; Zhang, J.; Shi, Y.; Pan, L. High-accuracy dynamic gesture recognition: A universal and self-adaptive deep-learning-assisted system leveraging high-performance ionogels-based strain sensors. *SmartMat* **2024**, e1269.
(37) Tie, J.; Mao, Z.; Zhang, L.; Zhong, Y.; Xu, H. Stretchable, Self-Healing, and Remodelable Ionogel via In Situ Phase Separation as a Highly Sensitive Multimode Sensor. *ACS Appli. Polym. Mater.* **2023**, *5* (11), 9092-9102.

(38) Peng, H.; Yang, F.; Wang, X.; Feng, E.; Sun, K.; Hao, L.; Zhang, X.; Ma, G. Rapid Radiation Synthesis of a Flexible, Self-Healing, and Adhesive Ionogel with Environmental Tolerance for Multifunctional Strain Sensors. *ACS Appli. Mater. Interfaces* **2023**, *15* (44), 51763-51773.
(39) Luo, C.; Chen, Y.; Huang, Z.; Fu, M.; Ou, W.; Huang, T.; Yue, K. A Fully Self-Healing and Highly Stretchable Liquid-Free Ionic Conductive Elastomer for Soft Ionotronics. *Adv. Funct. Mater.* **2023**, *33* (49), 2304486.
(40) Zhou, R.; Jin, Y.; Zeng, W.; Jin, H.; Shi, L.; Bai, L.; Shang, X. Versatile Quasi-Solid Ionic Conductive Elastomer Inspired by Desertification Control Strategy for Soft Iontronics. *Adv. Funct. Mater.* **2023**, *33* (43), 2301921.
(41) Sun, L.; Huang, H.; Zhang, L.; Neisiany, R. E.; Ma, X.; Tan, H.; You, Z. Spider-Silk-Inspired Tough, Self-Healing, and Melt-Spinnable Ionogels. *Adv. Sci.* **2024**, *11* (3), 2305697.